INTERNATIONAL JOURNAL FOR NUMERICAL METHODS IN FLUIDS
Int. J. Numer. Meth. Fluids **29**: 229–248 (1999)

NUMERICAL STUDY ON THE VORTEX MOTION PATTERNS AROUND A ROTATING CIRCULAR CYLINDER AND THEIR CRITICAL CHARACTERS

GUO-PING LING[a] AND TSI-MIN SHIH[b,*]

[a] *Department of Mathematics, Suzhou University, Suzhou, 215006, China*
[b] *Department of Applied Mathematics, Hong Kong Polytechnic University, Hong Kong*

SUMMARY

A hybrid finite difference and vortex method (HFDV), based on the domain decomposition method (DDM), is used for calculating the flow around a rotating circular cylinder at Reynolds number $Re = 1000$, 200 and the angular-to-rectilinear speed ratio $\alpha \in (0.5, 3.25)$ respectively. A fully implicit third-order eccentric finite difference scheme is adopted in the finite difference method, and the deduced large broad band sparse matrix equations are solved by a highly efficient modified incomplete LU decomposition conjugate gradient method (MILU-CG). The long-time, fully developed features about the variations of the vortex patterns in the wake, as well as the drag and lift forces on the cylinder, are given. The calculated streamline contours are in good agreement with the experimentally visualized flow pictures. The existence of the critical state is confirmed again, and the single side shed vortex pattern at the critical state is shown for the first time. Also, the optimized lift-to-drag force ratio is obtained near the critical state. Copyright © 1999 John Wiley & Sons, Ltd.

KEY WORDS: finite difference method; incomplete LU decomposition; preconditioned conjugate gradient method; rotating circular cylinder; vortex method; vortex pattern

1. INTRODUCTION

The unsteady flow around a rotating circular cylinder is a typical kind of complex fluid flow. It includes many complicated flow phenomena, such as the unsteady boundary layer separation, the generation and shedding of vortices, and their interactions with wakes, etc. The rotation of a circular cylinder about its axis will decrease and suppress the flow separation and vortex shedding on one side of the cylinder, while increase and develop them on another side. A transverse lift force will act on the cylinder, and this phenomenon is called the Magnus effect. The most important parameter for the case is the angular-to-rectilinear speed ratio α ($= \Omega a / U_\infty$, where Ω is the angular speed of the cylinder, a is the radius of the cylinder and U_∞ is the ambient flow velocity at infinity). The variation of a will effectively change the vortex pattern in the wake, as well as the drag and lift forces on the cylinder. One of the important objectives in current flow control research is to study the effect of cylinder rotation, to which great attention has been paid by many fluid mechanists world-wide.

Early research works were only for flow regions with small a and low Reynolds number Re ($= U_\infty \cdot 2a/v$, where v is the kinetic viscosity of the fluid). Since the 1980s, a series of

---

[*] Correspondence to: Department of Applied Mathematics, Hong Kong Polytechnic University, Hong Kong.

CCC 0271–2091/99/020229–20$17.50

Received February 1997
Revised November 1997

experimental [1–3] and numerical [3–6] studies have been carried out for some flow regions with larger a and higher Re. However, there are some issues regarding whether the vortex shedding will be suppressed and disappear completely while the flow is approaching steady. It has been shown [5] that the rotation does not suppress vortex shedding, even for $Re = 200$, $a = 3.25$. After the first main vortex (i.e. the initial starting vortex), the second and third (and so on) vortices also shed from the same side of the cylinder (called the single side vortex shedding). This contradicts the experimental results of [1], which indicate that after the first main vortex, the flow tends to be steady and the vortex shedding disappears completely. Recently, a systematic numerical study on the flow around a rotating circular cylinder for $Re = 1000$, $a \in (0.5, 6)$ was preformed [7], the results of which support the conclusions in [1], but do not give more details about the flow characters at the critical states.

The vortex method (VM) and the finite difference method (FDM) are the two major methods for numerical simulation of a bluff body's separated flow. The VM can effectively predict the global features of unsteady separated flow and the flow field structures away from the vorticity layer. But in the boundary layer or the shear layer, where viscous effects dominate convective effects, the diffusion of vorticity is usually simulated by the random walk of vortices in the method, and the fluctuations in numerical results are inevitable. In order to improve the precision of the computation, some smooth techniques must be introduced, especially in predicting the flow separation and vorticity distribution near or on the body surface. Meanwhile, the number of vortices must be very large. This will greatly increase the size of the computation. This difficulty can be overcome by the vortex-in-cell method (VIC), which reduces the size of the computation from the order of $O(N^2)$ (N is the number of vortices) to $O(N \log_2 N)$. Another drawback of the VM is that boundary conditions cannot be easily prescribed. In the near-wake of the bluff body, due to the reverse flow, some discrete vortices may cross the body surface during a time step. How to deal with these vortices is somewhat arbitrary. Conversely, the FDM can efficiently yield very precise results for the N–S equations at moderate Reynolds numbers, with various forms of boundary conditions; especially in the regions where viscous effects dominate convective effects. But when the Reynolds number increases, the number of nodes will rapidly increase, and the cost of the computation will be impractically high. In addition, there are still some theoretical problems to be solved in the finite difference solution to the flow at high Reynolds numbers.

After considering both the advantages and existing problems of the two methods mentioned above, a hybrid finite difference and vortex method (HFDV), based on the domain decomposition method (DDM), is adopted. The similar method, the so-called the partial-grid domain decomposition method or the partical-grid superposition method, was first proposed by Cottet [8], then developed by Guermond [9] and Chou [10] in successfully calculating the bluff body separated flows. But the methodology used here was proposed by the author [11], which is similar to work of Guermond. The flow field is divided into two domains: the inner domain and the outer domain. In the inner domain, the FDM is adopted. It can precisely treat the fine structures of the near-wake flow, and the amount of computation is moderate because the calculation region is restricted to the close neighborhood of the body. In the outer domain, the VIC method is used. It can effectively deal with the far-wake flow, where the viscosity is not dominant, and can be even neglected, especially at high Reynolds numbers. In the computation results, the fluctuation caused by the random walk of vortices is limited, and the difficulty caused by vortices crossing the body surface does not exist. Therefore, this hybrid combination of the finite difference and vortex methods has the advantages of both methods, while avoiding their defects. This method has been successfully applied to calculate the impulsively started flow [11,12] and the oscillating flow [13,14] around a circular cylinder.

When the flow complexity increases, more effective, stable and accurate numerical methods must be developed. Finer grids and higher-order implicit difference algorithms should be adopted. It will produce a kind of large broad band (more than three diagonals) matrix equations. For these equations, some traditional methods in CFD, such as the ADI, LSOR or SIP methods, are not valid or efficient any longer. An advanced, effective conjugate gradient method with modified incomplete LU decomposition as preconditioner (MILU-CG) is adopted instead. It can quickly solve the broad band matrix equations, and no alternate directional iteration process is needed. It is one of the most updated algorithms in large-scale scientific and engineering computations [15]. The MILU-CG method combined with the modified HFDV method is used for calculating the flow around a rotating circular cylinder at $Re = 1000$, 200, $\alpha \in (0.5, 3.25)$ for studying the variation rules of vortex patterns and forces in long-time periods, from the start to fully developed. The calculated streamline contours are in good agreement with the experimentally visualized flow pictures. The existence of the critical state is confirmed again, and the single side shed vortex pattern at the critical state is given for the first time. The maximum lift-to-drag force ratio is also determined near the critical states.

2. MATHEMATICAL MODEL

An incompressible and viscous fluid, with a uniform velocity U_∞ at infinity, is assumed to flow around a circular cylinder of radius a in the x-direction (see Figure 1). The cylinder rotates about its axis in the counter-clockwise direction with an angular velocity Ω. A polar co-ordinate system, whose origin coincides with the center of the cylinder, is chosen.

The dimensionless variables t, r, (V_r, V_θ), ψ and ω are obtained by being divided by a/U_∞, a, U_∞ $U_\infty a$ and U_∞/a respectively. The dimensionless governing equations of the flow, in terms of vorticity (ω) and streamfunction (ψ), are as follows:

$$\frac{\partial \omega}{\partial t} + \frac{1}{r}\frac{\partial}{\partial r}(rV_r\omega) + \frac{1}{r}\frac{\partial}{\partial \theta}(V_\theta\omega) = \frac{2}{Re}\nabla^2\omega, \tag{1}$$

$$\nabla^2\psi = -\omega, \tag{2}$$

where $V_r = \partial\psi/r\,\partial\theta$, $V_\theta = -\partial\psi/\partial r$ are the radial and peripheral velocities respectively.

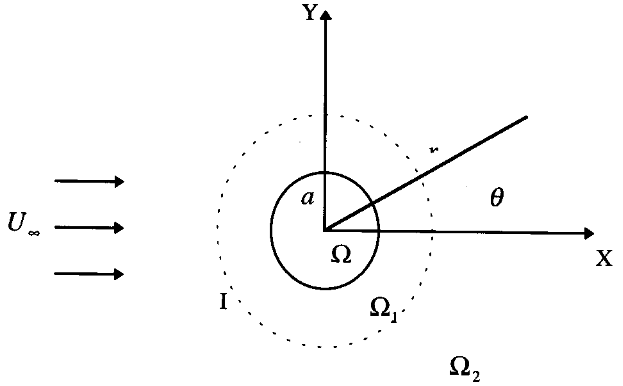

Figure 1. Flow sketch and domain decomposition.

In order to have finer meshes in the vicinity of the cylinder surface, a log–polar co-ordinate system is introduced, i.e. $r = \exp(2\pi\xi)$, $\theta = 2\pi\eta$. The dimensionless governing equations of the flow then change to:

$$E\frac{\partial\omega}{\partial t} + \frac{\partial}{\partial\xi}(U\omega) + \frac{\partial}{\partial\eta}(V\omega) = \frac{2}{Re}\left(\frac{\partial^2\omega}{\partial\xi^2} + \frac{\partial^2\omega}{\partial\eta^2}\right), \tag{3}$$

$$\frac{\partial^2\psi}{\partial\xi^2} + \frac{\partial^2\psi}{\partial\eta^2} = -E\omega, \tag{4}$$

where $E = 4\pi^2\exp(4\pi\xi)$, $U = \partial\psi/\partial\eta = E^{1/2}V_r$ and $V = -\partial\psi/\partial\xi = E^{1/2}V_\theta$.

On the surface of the cylinder, the no-slip condition of impermeable wall must be satisfied, i.e.

$$\begin{cases} \psi = 0, \quad \dfrac{\partial\psi}{\partial\xi} = -E^{1/2}\alpha & \\ & \xi = 0, \\ \omega = -\dfrac{1}{E}\dfrac{\partial^2\psi}{\partial\xi^2}, & \end{cases} \tag{5}$$

and at infinity, the influence of rotation on the flow field can be neglected,

$$\begin{cases} \dfrac{\partial\psi}{\partial\xi} = E^{1/2}\sin(2\pi\eta), & \\ & \xi \to \infty. \\ \dfrac{\partial\omega}{\partial\xi} = 0, & \end{cases} \tag{6}$$

The initial condition is

$$\omega|_{t=0} = 0, \qquad \xi > 0. \tag{7}$$

After the vorticity distribution in the field is obtained from Equations (3)–(7), one can deduce the distributions of the pressure and shear stress on the cylinder surface, as well as the drag and lift force coefficients C_d and C_l,

$$\begin{cases} C_\mathrm{d} = \dfrac{2}{Re}\displaystyle\int_0^1 \left(\frac{\partial\omega}{\partial\xi} - 2\pi\omega\right)\bigg|_{\xi=0} \cdot \sin(2\pi\eta)\cdot \mathrm{d}\eta, \\ C_\mathrm{l} = -\dfrac{2}{Re}\displaystyle\int_0^1 \left(\frac{\partial\omega}{\partial\xi} - 2\pi\omega\right)\bigg|_{\xi=0} \cdot \cos(2\pi\eta)\cdot \mathrm{d}\eta, \end{cases} . \tag{8}$$

3. NUMERICAL METHODS

3.1. The domain decomposition method

The entire flow field is decomposed into two domains: the inner domain Ω_1, which is close to the body surface, and the outer domain Ω_2, which covers the rest of the field. The interface between Ω_1 and Ω_2 is I, as shown in Figure 1.

The flow in the inner domain Ω_1 is viscous-dominant, where the flow separation and vortex shedding occur. In Ω_1, the variation of vorticity and the flow field are determined by the N–S equation and the Poisson equation about streamfunctions with corresponding initial and boundary conditions. The FDM is used for calculating the flow field. In domain Ω_2, the flow is assumed to be approximately inviscid. The convection of the vortex is calculated by the discrete vortex model and the VIC method. The vorticity is conserved when the vortex is in motion. The velocity of the motion is given by the Poisson equation.

The flows in the two domains are coupled through the interface I, and will be solved simultaneously. The outer domain gains the newly generated discrete vortex from the vorticity flux passing across the interface, which serves as the added source term at each time step for solving the vortex motion in this domain. In solving the flow field of the inner domain, the boundary conditions of ω and ψ at the interface are given by interpolating the corresponding values on nodes near the interface.

The inner domain is bounded in the range of $r = O(a)$. This range may be determined flexibly through numerical tests according to the accuracy required when describing the fine structure of the flow and the size of the computation. In this computation, the interface between the inner and outer domains is located at $r \simeq 3a$ (following [11]).

3.2. *The finite difference method*

In domain Ω_1, the flow field is calculated by a predictor–corrector type of FDM. At the prediction stage, the value of ω at the $(n+\frac{1}{2})$th time step, $\omega^{(n+1/2)}$, is obtained by solving the Equation (3) with the values of ω, U and V at the (n)th time step, $\omega^{(n)}$, $U^{(n)}$ and $V^{(n)}$. Equation (3) is discretized by using of the first-order upwind difference scheme for the convection terms and the second-order central difference scheme for the viscous terms. Having got $\omega^{(n+1/2)}$, one can calculate the value of $\psi^{(n+1/2)}$ by using Equation (4) and then the values of $U^{(n+1/2)}$ and $V^{(n+1/2)}$, where Equation (4) is discretized by the second-order central difference scheme also. The traditional alternating direction implicit (ADI) method and the line successive overrelaxation (LSOR) method are used in calculating Equations (3) and (4) respectively. Here, the coefficient matrices of the deduced finite difference equations are three-diagonal, so the computation is rapid, but the precision is only of first-order in time and first- or second-order in space. The reason why the algorithms mentioned above were used as the predictor is that the computer codes have already operated effectively in previous works by the authors [11,12].

At the correction stage, the third-order eccentric finite difference scheme is adopted for the convection terms of Equation (3). For example, the discrete form of $\partial/\partial\xi\ (U\omega)$ is as follows:

$$\frac{\partial}{\partial \xi}(U\omega) = \begin{cases} ((U\omega)_{i+2,j} - 2(U\omega)_{i+1,j} + 9(U\omega)_{i,j} - 10(U\omega)_{i-1,j} + 2(U\omega)_{i-2,j})/6\Delta\xi, & U_{i,j} > 0, \\ (-2(U\omega)_{i+2,j} + 10(U\omega)_{i+1,j} - 9(U\omega)_{i,j} + 2(U\omega)_{i-1,j} - (U\omega)_{i-2,j})/6\Delta\xi, & U_{i,j} < 0. \end{cases} \tag{9}$$

Equation (4) and the viscous terms of Equation (3) are also discretized by the second-order central difference scheme. The difference form for time advance in Equation (3) is implicit, which can be expressed as

$$E\frac{\omega^{(n+1)} - \omega^{(n)}}{\Delta t} = f\left(\frac{1}{2}(\omega^{(n+1)} + \omega^{(n)}),\ U^{(n+1/2)},\ V^{(n+1/2)}\right), \tag{10}$$

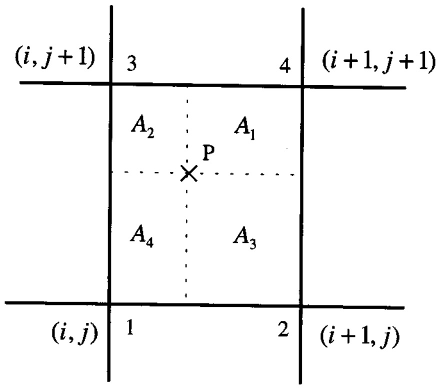

Figure 2. Area weighting scheme.

where $f(\omega, U, V)$ denotes all the terms moved to the right side of Equation (3), $U^{(n+1/2)}$ and $V^{(n+1/2)}$ denote the corresponding values at the $(n+\frac{1}{2})$th time step, which are already obtained at the prediction stage. Now the precision is of second-order in time and second- or third-order in space, but the coefficient matrices of the deduced finite difference equations are of nine-diagonal and of five-diagonal. Some more efficient numerical algorithms for solving such kinds of broad band matrix equations must be developed.

The preconditioned conjugate gradient method (PCG) is a kind of most effective algorithms for solving large broad band sparse matrix equations [15]. Its efficiency depends on the preconditioner. A good preconditioner is a matrix M, which satisfies the following two conditions: (1) the inverse of M can be easily obtained, and (2) the condition number of $M^{-1}A$ should be much less than that of the original matrix A. The procedure of the PCG is as follows:

```
$X := X^0$
$g := AX - b$;      $h := M^{-1}g$
$d := -h$;      $\delta_0 := g^T h$
if $\delta_0 \leq \varepsilon$ then stop
$R$: continue
$h := Ad$
$\tau := \delta_0/(d^T h)$
$X := X + \tau d$
$g := g + \tau h$
$h := M^{-1}g$
$\delta_1 := g^T h$
if $\delta_1 \leq \varepsilon$ then stop
$\beta := \delta_1/\delta_0$;      $\delta_0 := \delta_1$
$d := -h + \beta d$
goto $R$.
```

One of the popular preconditioners is the incomplete LU decomposition (ILU). A subscript set $S_A = \{(i, j): a_{i,j} \neq 0\}$ is defined. If a LU decomposition is only carried out on those $a_{i,j}$ whose subscripts belong to S_A, this kind of decomposition is called an ILU decomposition. Because of the sparseness of A, the number of the elements in S_A is small. So the computation cost of ILU is less than that of LU. If the neglected terms $-a^r_{ir}a^r_{rj}$, $(i, j) \in S_A$ are added to the diagonal elements a^r_{ii}, a more effective modified version of ILU, the so-called MILU, is formed. The procedure of MILU is as follows:

```
$A^0 := A$
for $r := 1$ to $n$ do
begin
  for $j \geq r$ and $(i, r) \in S_A$ do
    $a^r_{rj} := a^{r-1}_{rj}$
  for $i > r$ and $(i, r) \in S_A$ do
    $a^r_{ir} := a^{r-1}_{ir} / a^r_{rr}$
  for $i, j > r$ and $(i, r) \in S_A$ and $(r, j) \in S_A$ do
    begin
      $q := -a^r_{ir}a^r_{rj}$
      if $(i, j) \in S_A$ then $a^r_{ij} := a^{r-1}_{ij} + q$
      else $a^r_{ii} := a^r_{ii} + q$
    end
end.
```

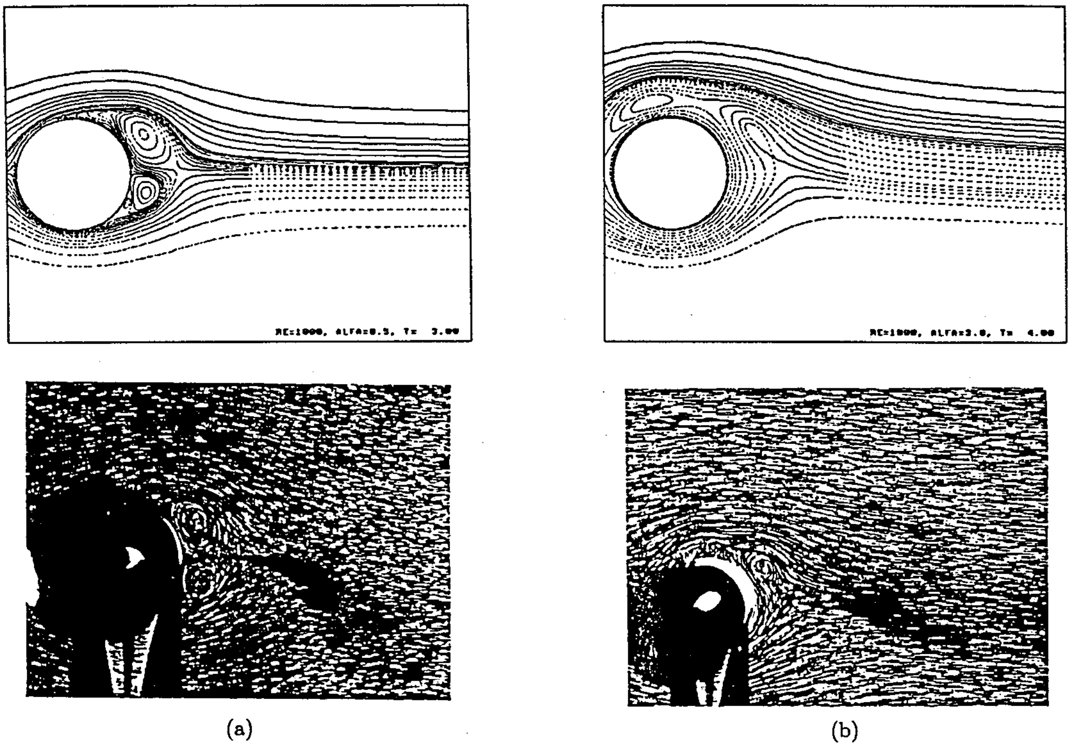

Figure 3. Comparisons of the calculated streamline contours with the experimental visualization for $Re = 1000$, (a) $\alpha = 0.5$, $t = 3$; (b) $\alpha = 3$, $t = 4$.

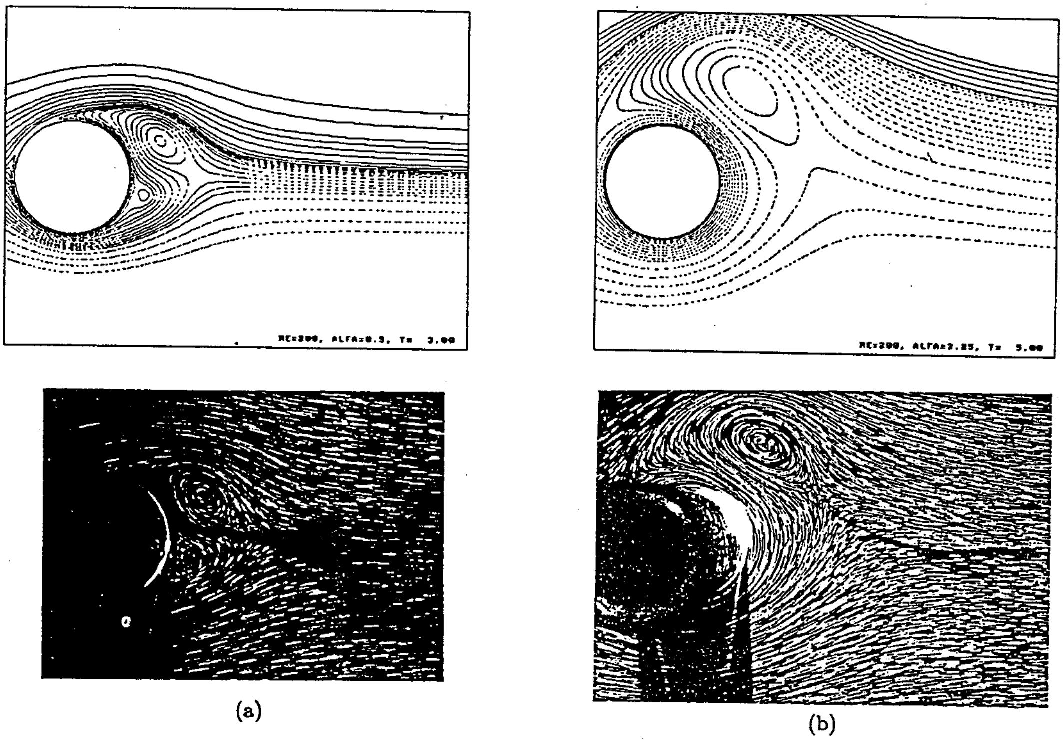

(a)

(b)

Figure 4. Comparisons of the calculated streamline contours with the experimental visualizations for $Re = 200$, (a) $\alpha = 0.5$, $t = 3$; (b) $\alpha = 3.25$, $t = 5$.

For $(i, j) \in S_A$, a^r_{ij} will appear in a lower triangular matrix L $(i < j)$ or an upper one U $(i \geq j)$ respectively. The inversion of the preconditioned matrix $M = LU$ can be obtained through a simple forward and backward substitution procedure.

The conjugate gradient method with MILU as its preconditioner, i.e. MILU-CG, has been successfully applied to oil reservoir simulations, and shown that the calculation speed is about seven or eight times faster than that of the LSOR [16]. Hence the MILU-CG method is used here.

3.3. The vortex method

In domain Ω, the flow field is calculated by the VIC method. The amount of vorticity transported from the inner domain to the outer one is determined by the vorticity flux across the interface. The strength of a nascent discrete vortex, passing through the jth section of the interface I during a time step Δt, may be expressed as

$$\Delta\Gamma_j = \int_j \omega_I U_n \, d\eta \cdot \Delta t, \tag{11}$$

where U_n is the normal velocity at the interface. After Δt, each nascent discrete vortex will be located at

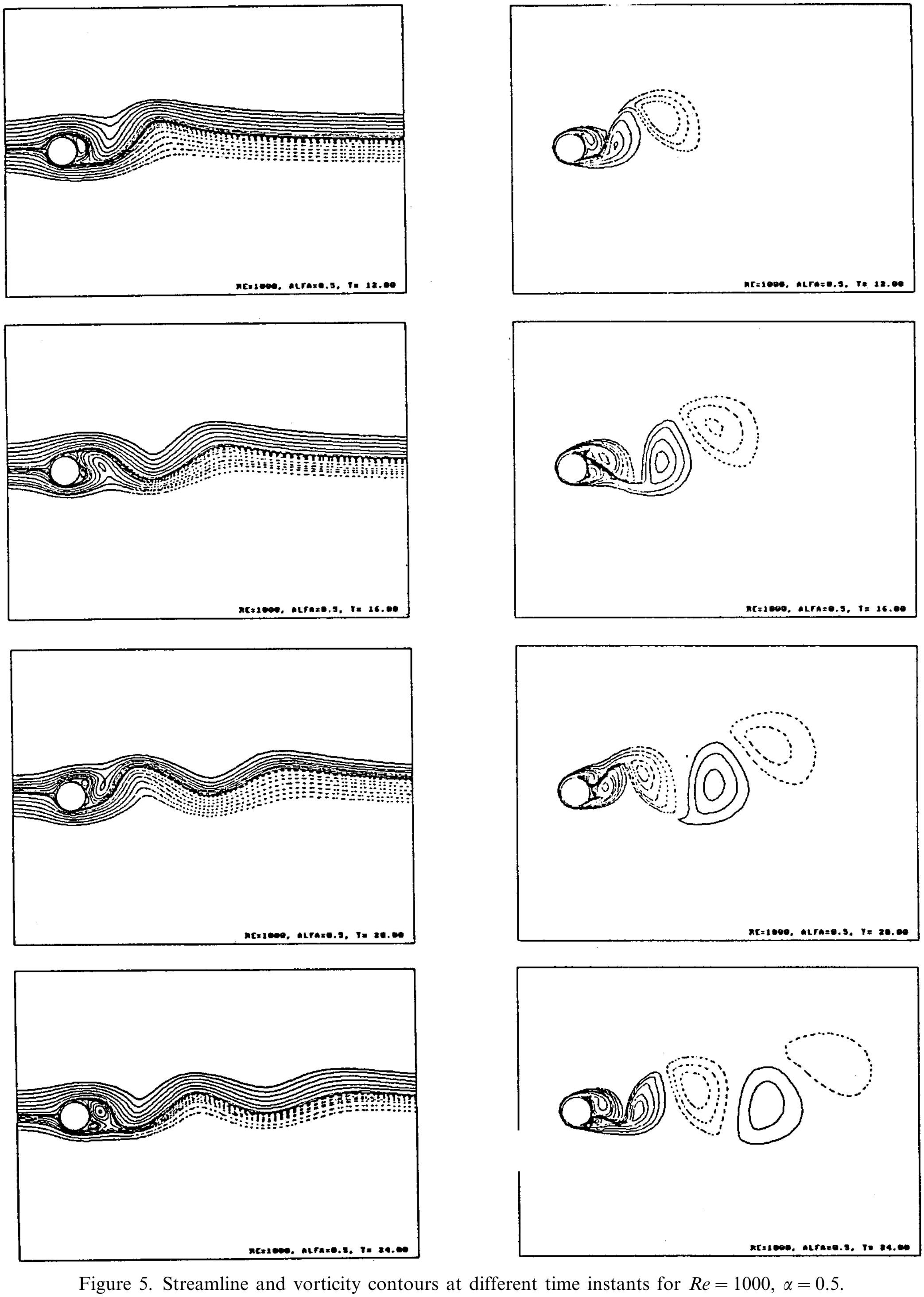

Figure 5. Streamline and vorticity contours at different time instants for $Re = 1000$, $\alpha = 0.5$.

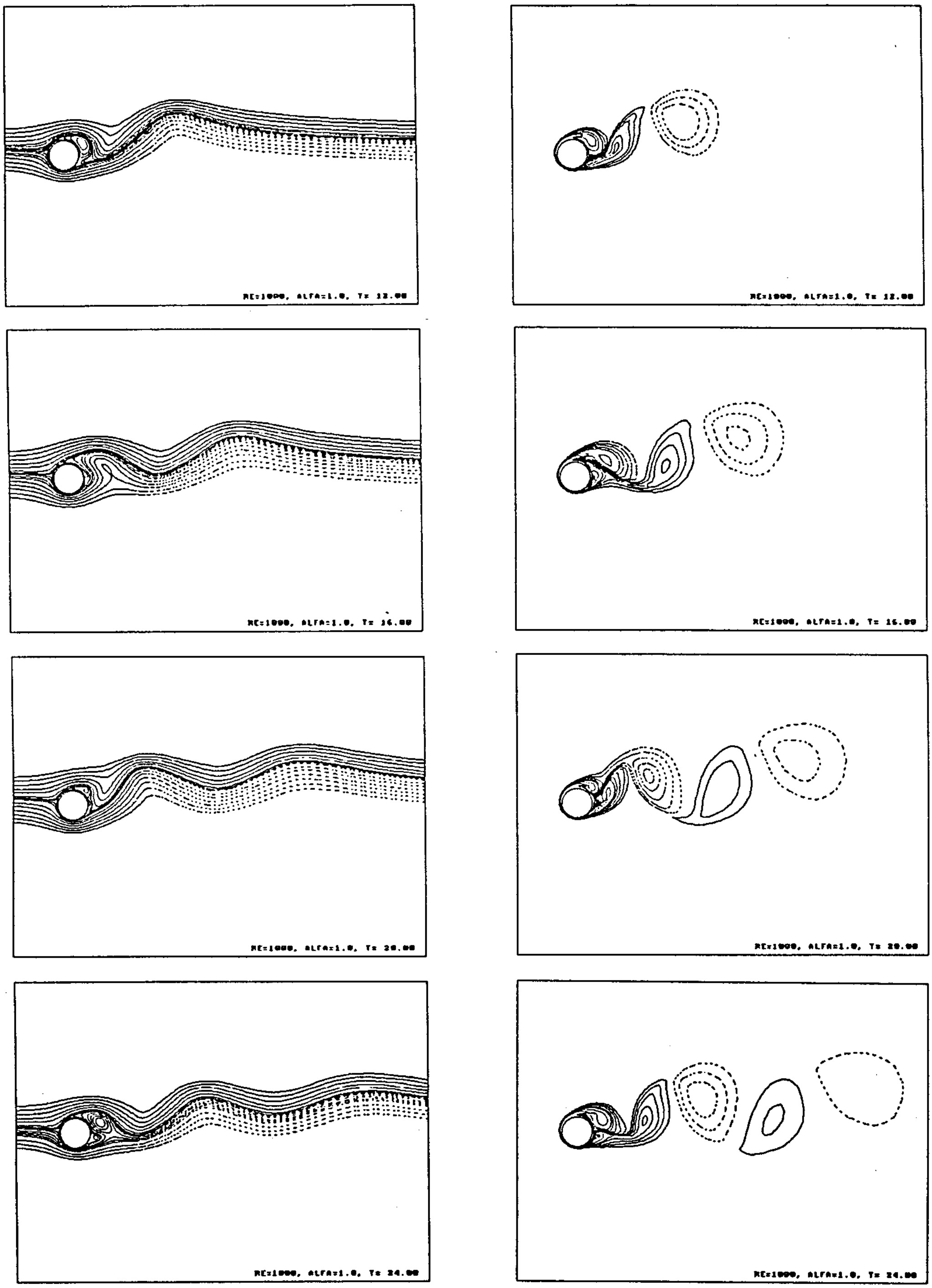

Figure 6. Streamline and vorticity contours at different time instants for $Re = 1000$, $\alpha = 1$.

$$\begin{cases} \xi(t+\Delta t) = \xi(t, I) + \delta\xi, \\ \eta(t+\Delta t) = \eta(t, j+\frac{1}{2}) + \delta\eta, \end{cases} \tag{12}$$

where

$$\begin{cases} \delta\xi = \dfrac{1}{2}\, U_I \cdot \Delta t/E, \\ \delta\eta = \dfrac{1}{2}\, V_I \cdot \Delta t/E. \end{cases}$$

In the outer region after Δt, the position of the old discrete vortex can be determined by

$$\begin{cases} \xi(t+\Delta t) = \xi(t) + \delta\xi, \\ \eta(t+\Delta t) = \eta(t) + \delta\eta, \\ \delta\xi = U_{\mathrm{p}} \cdot \Delta t/E, \\ \delta\eta = V_{\mathrm{p}} \cdot \Delta t/E, \end{cases} \tag{13}$$

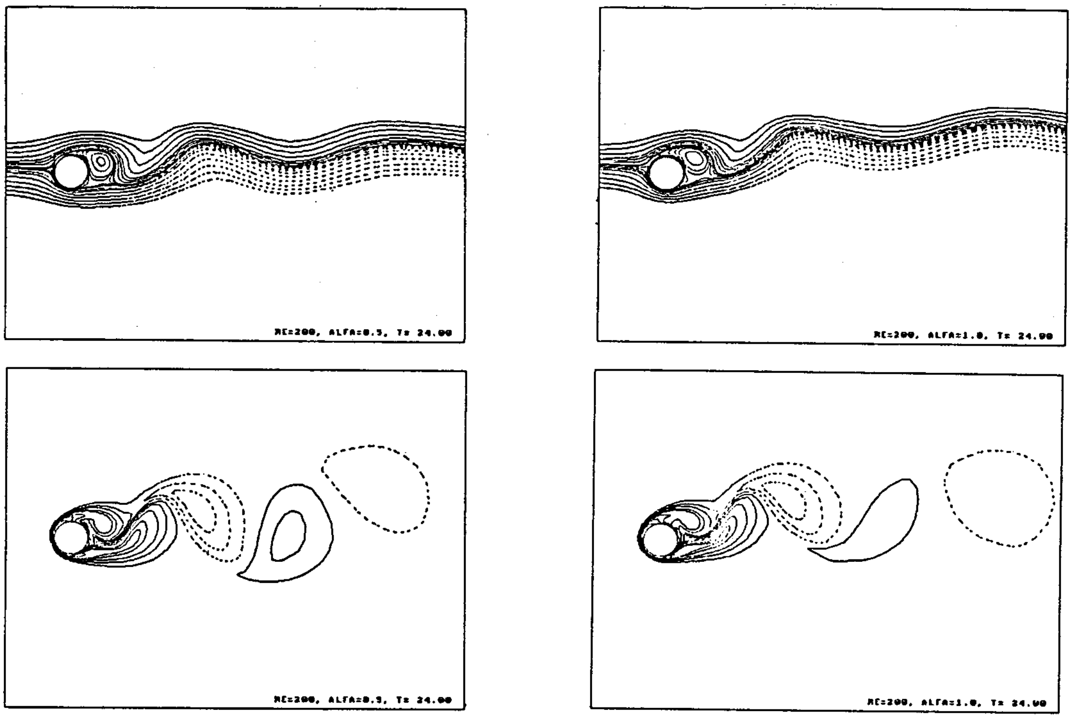

(a) (b)

Figure 7. Streamline and vorticity contours at $t = 24$ for $Re = 200$, (a) $\alpha = 0.5$; (b) $\alpha = 1$.

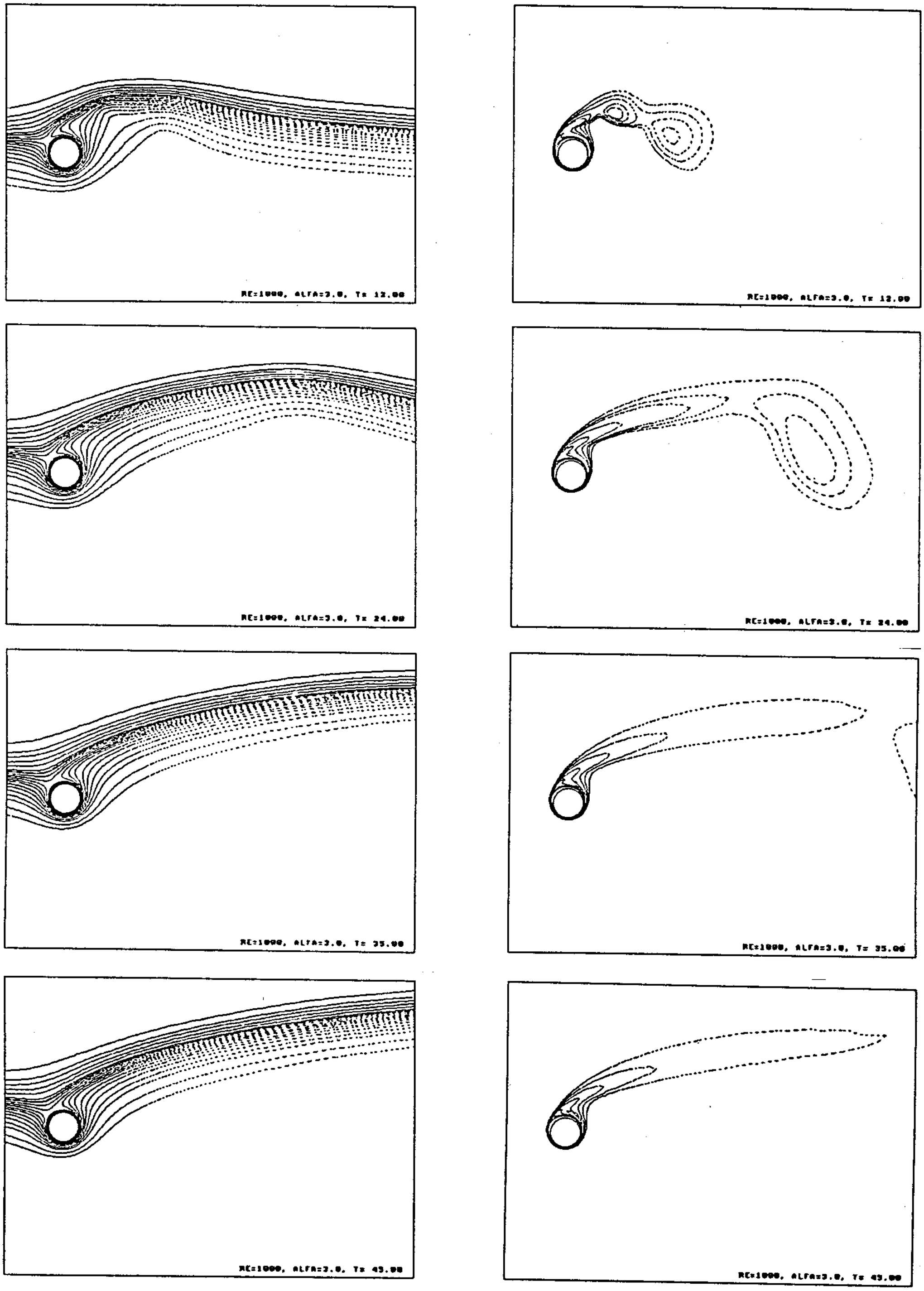

Figure 8. Streamline and vorticity contours at different time instants for $Re = 1000$, $\alpha = 3$.

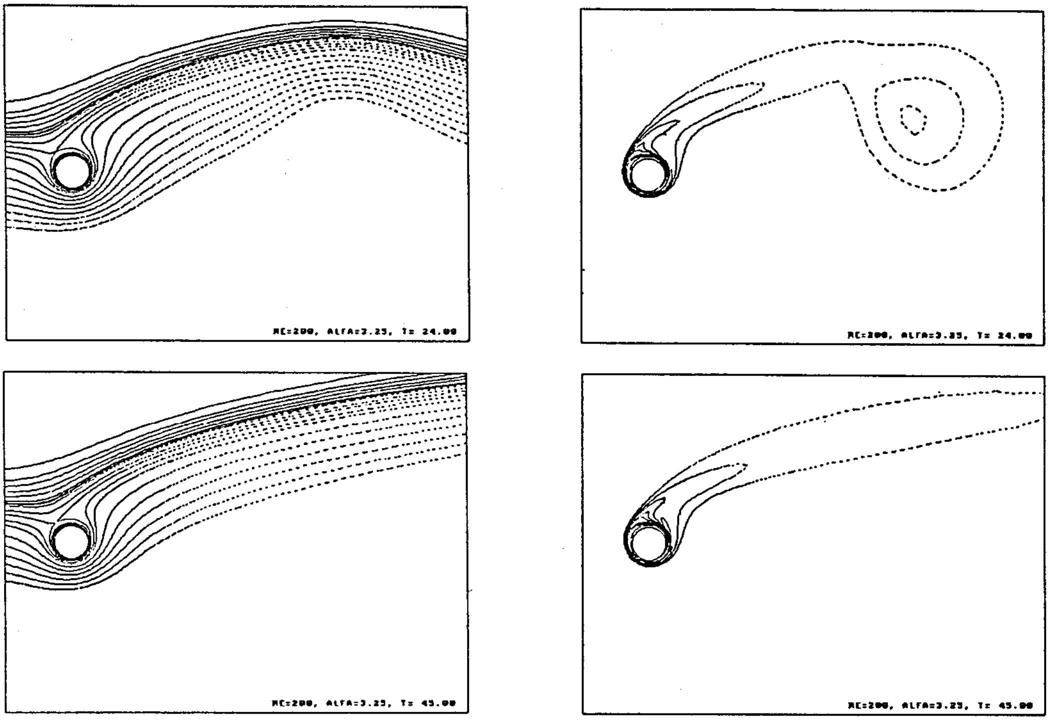

Figure 9. Streamline and vorticity contours at $t = 24$ and 45 for $Re = 200$, $\alpha = 3.25$.

where U_{p} and V_{p} are velocities of the old discrete vortex. These velocities are obtained by using an area weighting method as follows:

$$\begin{cases} U_{\mathrm{p}} = \sum\limits_{k=1}^{4} u_k A_k / A, \\ V_p = \sum\limits_{k=1}^{4} v_k A_k / A, \end{cases} \tag{14}$$

where u_k and v_k are flow field velocities on grid nodes, and A is the area of the cell occupied by the vortex (see Figure 2). When the vortex with strength Γ reaches its new position, the corresponding vorticity contribution to grid nodes is

$$\omega_k = \frac{\Gamma}{E_k} \frac{A_k}{A^2}, \quad k = 1, 2, 3, 4. \tag{15}$$

The area weighting method is essentially a bilinear interpolation scheme, whose disadvantage is having to account for grid effects. One way to reduce the influence of the grid is to use other more accurate weighting functions or filters, e.g. the Couet filter, etc. [17]. But in the computations here this kind of grid-dependence is not substantial as usual, because the VIC method is just used in the outer domain's calculations. The influence of the grid on the vortex shedding frequency, drag and lift forces is small when fine meshes are used in the calculations. The grid size used here is determined through numerical tests, by refining meshes when the difference among the values of the drag and lift forces on the different sizes of grids is $< 1\%$. So the calculated results may be regarded as almost grid-independent.

3.4. The computation procedure

The inner domain and the whole flow field are divided into fine and coarse grids respectively. Both fine and coarse grids are applied simultaneously to the inner domain. The computation procedure is as follows:

(1) Given the variables on the interface at the nth time step, solve the N–S equations on the fine grid and obtain the vorticity distribution in Ω_1.

(2) Calculate the nascent discrete vortex transferring into Ω_2 and the movement of the old discrete vortex already existing there. Obtain the vorticity distribution in Ω_2.

(3) Solve the Poisson equation and obtain the streamfunction and the velocity distributions on the coarse grid.

(4) Calculate the vorticity, the streamfunction and the velocity distributions on the interface.

(5) Solve the Poisson equation on the fine grid to obtain the streamfunction and then the velocity distributions in Ω_1. Calculate the vorticity distribution on the cylinder surface, as well as the drag and lift forces.

Repeat the steps (1)–(5) to the end-time of the computation.

4. RESULTS AND DISCUSSION

The flows around an impulsively started rotating circular cylinder for $\alpha \in (0.5, 3.25)$ with $Re = 1000$ and 200, are simulated respectively. Fine grids are applied to the inner domain, where the total number of nodes is 144×240, and the corresponding domain on the physical plane is $a \leq r \leq 3a$, $\theta \leq 2\pi$. Coarse grids are applied to the whole domain, where the total number of nodes is 300×240, and the corresponding domain on the physical plane is $a \leq r \leq 110a$, $0 \leq \theta \leq 2\pi$. The time step is $\Delta t = 0.01$, and the end-time is $t = 80$.

In Figures 3 and 4, the calculated streamline contours are compared with the experimental visualizations [1–3,6]. Figure 3 shows cases for $Re = 1000$ with (a) $\alpha = 0.5$, $t = 3$ and (b) $\alpha = 3$, $t = 4$. Figure 4 shows cases for $Re = 200$ with (a) $\alpha = 0.5$, $t = 3$ and (b) $\alpha = 3.25$, $t = 5$. The good agreements have verified the accuracy of the present numerical methods.

By changing α, different vortex patterns will be presented in the wake of the cylinder.

Figure 5 shows the streamline and vorticity contours at different times for $Re = 1000$ and $\alpha = 0.5$. The rotation of the cylinder creates asymmetry in the formation of the wake flow behind it. The first clockwise negative vortex is formed and shed from the upper side of the cylinder, then the second anti-clockwise positive vortex is formed and shed from the lower side, and so on. A periodical alternate shed vortex pattern is presented in the wake, just like the Von Karman vortex street in the stationary cylinder case ($\alpha = 0$). The streamline contours are periodically fluctuated, and look like a traveling wave. Their central lines are deflected upwards in the rotating direction. When $\alpha = 1$ (Figure 6), the steamline and vortex evolution patterns are found to be basically the same as those for $\alpha = 0.5$, as are those for the cases of $Re = 200$, $\alpha = 0.5$ and 1 (Figure 7).

Figure 8 shows the streamline and vorticity contours at different times for $Re = 1000$ and $\alpha = 3$. The increase in α tends to decrease the process of the anti-clockwise positive vortex formation on the lower side of the cylinder. Now α is sufficiently large, and the development of the vortex on the lower side is fully suppressed. The time taken for the first main vortex to be shed from the upper side is longer than that for $\alpha \leq 1$. After the first main vortex is shed, the flow tends to steady. There are no other vortices shed from the cylinder besides the vortex attached to the upper side. The wavy streamlines of periodic fluctuation cease to develop. Some closed streamlines appear around the cylinder surface. After the first wave is passed, the streamlines become flatter and are deflected upward more substantially. For the case of $Re = 200$ and $\alpha = 3.25$ (Figure 9), the situation is the same. These results are in agreement with the experimental results in [1,3], and the numerical results in [7].

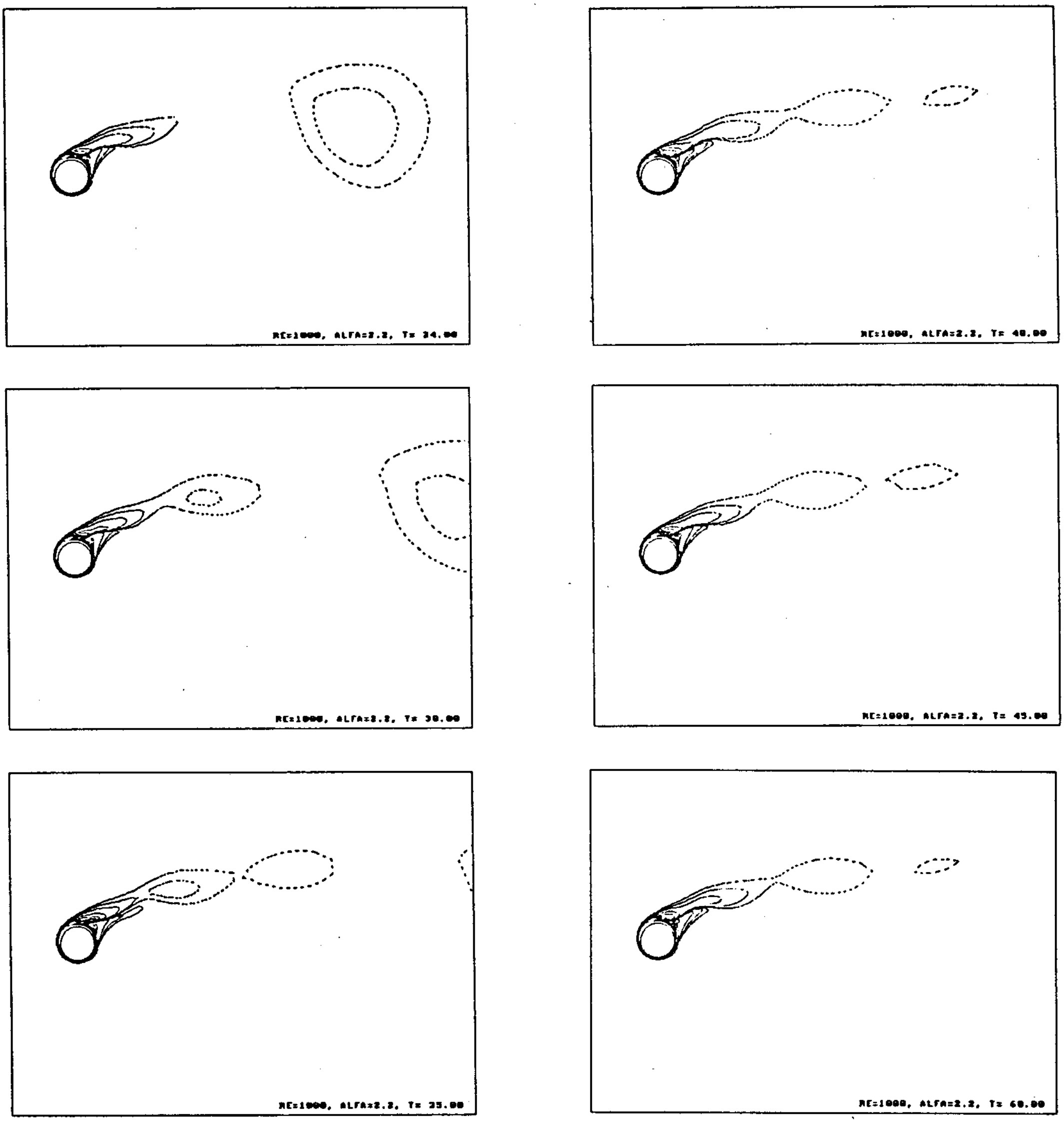

Figure 10. Vorticity contours at different time instants for $Re = 1000$, in the critical state $\alpha_c = 2.2$.

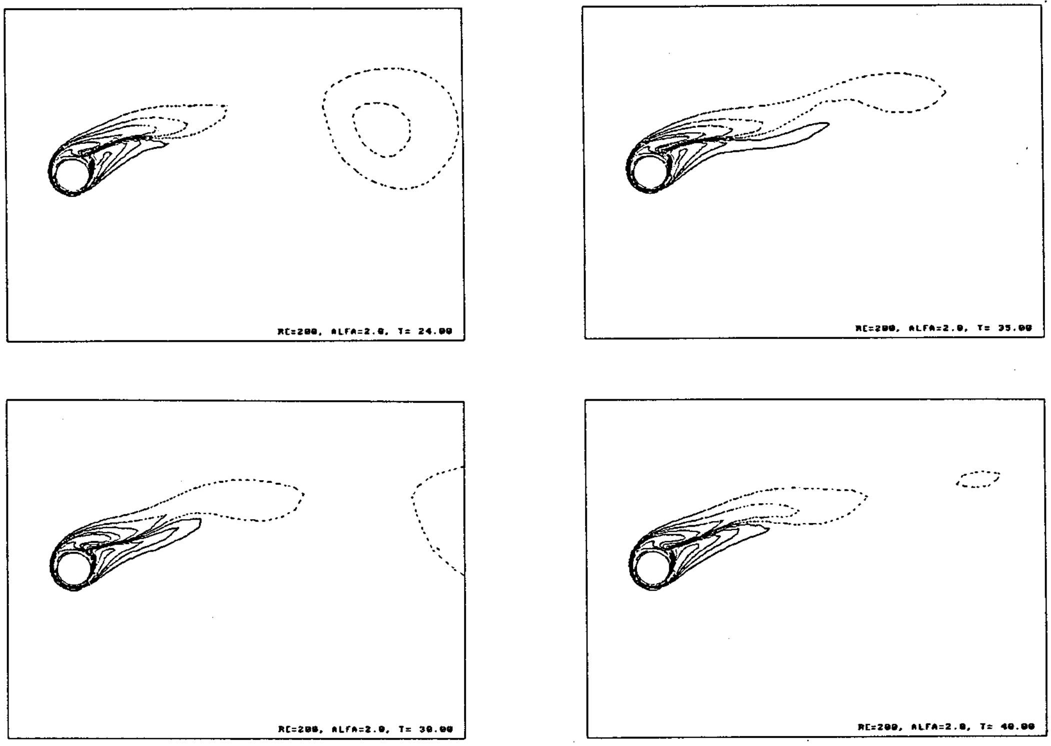

Figure 11. Vorticity contours at different time instants for $Re = 200$, in the critical state $\alpha_c = 2$.

There should exist a transition state, the so-called critical state, between the state of periodically alternate double side shed vortex pattern for smaller α and the state of steady single side attached vortex pattern for larger α. The existence of the critical states, which was indicated before [3,5,7], is confirmed here again. But so far, little is known about the flow character and vortex patterns in the critical states. Through numerical tests, the critical speed ratio α_c is found to be 2.2 and 2.0 for $Re = 1000$ and 200 respectively, and the character of the vortex patterns in critical states are given for the first time. Figure 10 shows the vorticity contours at different times in the critical state for $\alpha_c = 2.2$ for $Re = 1000$. The strength of the vortex shed from the lower side is so decreased that the vortex does not need to be shown in the plotting. But the vortex attached to the lower side still exists, having a periodical effect on the evolution of the upper side vortex. After the first main vortex is shed, the upper side vortex takes a shape like a 'lotus root', (not the flat shape as in the steady case shown in Figure 8). As time advances, parts of the 'lotus root' will shed one after the other. This is similar to the case of the single side shed vortex in [5], but now it takes place in the critical state, and not in the steady state. For $Re = 200$ (Figure 11), the vortex pattern in the critical state $\alpha_c = 2$ has a similar character.

The speed ratio α also has great influence on the drag and lift force coefficients. The variations of the drag and lift force coefficients, C_d and C_l, with respect to time for $Re = 1000$ and 200 are shown in Figures 12 and 13 respectively. When α is small ($= 0.5$, 1), the curves fluctuate with rather large amplitudes. The fluctuation frequencies for both C_d and C_l are the same. This is different from the case of a stationary cylinder ($\alpha = 0$), where the frequency of

C_d is twice that of C_l. When α is large enough ($=3, 3.25$), the curves tend to steady, and achieve their approximate values. When α is close to its critical value ($=2, 2.07$), the fluctuation amplitudes are very small, but the frequencies of C_d and C_l are still the same. One contradiction with some other numerical results [2,3,7] is that there seems some degree of negative Magnus effect during the early stage, which is called the overshoot phenomenon. This phenomenon is presented in many numerical simulations of flow around impulsively started translating cylinders, where the prediction of drag force during the early stage overshoots also. The initial flow field for impulsively started flow is taken to be of potential and the vorticity at $t=0^+$ is concentrated on the body surface in the form of a vortex sheet with infinitesimal thickness. Errors (overshoot phenomenon) are shown due to the inability of numerical schemes to resolve such an infinitesimal vorticity layer at $t=0^+$ [5]. Smaller initial time steps can be used to confine and reduce these errors to small times during the early stage. For example, in these calculations, $\Delta t=10^{-4}$ is used for $t\leq 0.3$, $\Delta t=10^{-3}$ for $0.3\leq t\leq 2$, and $\Delta t=10^{-2}$ for the rest. But the overshoot phenomenon still exists. So, whether the overshoot phenomenon is wrong or inherent and how to reduce it, need to be further investigated, especially by experiments. On the other hand, according to [18] even in the worst case of a body set impulsively into motion, the duration of the errors is confined to a limited time. This is confirmed by the present numerical tests; therefore, the long-term behaviors predicted here are not influenced by the errors. In Figure 14, the variations of (a) the mean drag force coefficient $\overline{C_d}$, (b) the mean lift force coefficient $\overline{C_l}$ and (c) the mean lift-to-drag force ratio $\overline{C_l}/\overline{C_d}$ with respect to α are shown. $\overline{C_l}$ increases almost linearly with increasing α. $\overline{C_d}$ also increases with

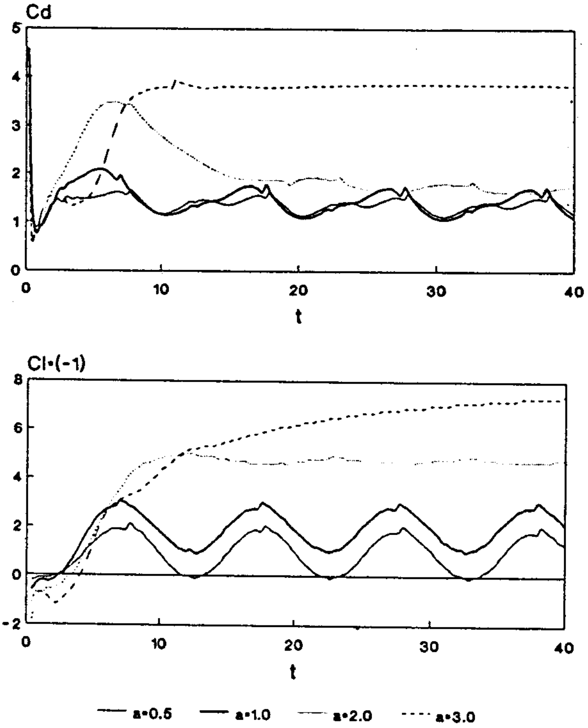

Figure 12. The variations of the drag and lift force coefficients, C_d and C_l, with respect to time t for $Re=1000$, $\alpha=0.5$, 1, 2 and 3.

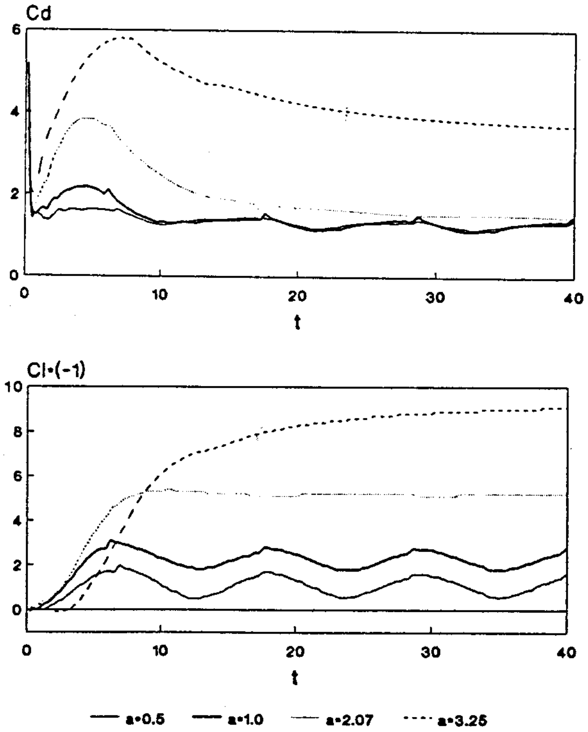

Figure 13. The variations of the drag and lift force coefficients, C_d and C_l, with respect to time t for $Re = 200$, $\alpha = 0.5$, 1, 2.07 and 3.25.

increasing α, but the increase in speed before or after the critical state is different, the latter is greater than the former. So, $\overline{C_l}/\overline{C_d}$ may reach its maximum value. The calculated results show that the maximum $\overline{C_l}/\overline{C_d}$ will be obtained near the critical state. This indicates the importance of studying the critical state of a rotating circular cylinder for the flow control problems.

5. CONCLUSIONS

(1) The speed ratio α has a dominant effect on the vortex patterns in the wake of a rotating circular cylinder, along with the drag and lift forces.

(2) There exists a critical state. When $\alpha < \alpha_c$, a periodical alternate double side shed vortex pattern occurs in the wake; the C_d and C_l fluctuate synchronously with time in rather large amplitudes. When $\alpha > \alpha_c$, a steady single side attached vortex pattern occurs; the C_d and C_l approach their steady values. When $\alpha \approx \alpha_c$, a lotus-root-like single side shed vortex pattern occurs; the C_d and C_l fluctuate synchronously with time in very small amplitudes.

(3) The maximum lift-to-drag force ratio is obtained near the critical state.

(4) The modified HFDV method used here is an efficient and accurate numerical method for calculating the separated flow around bluff bodies at moderate or high Reynolds numbers.

(5) For large broad band sparse matrix equations deduced from higher-order implicit finite difference algorithms, a kind of efficient preconditioned conjugate gradient methods, e.g. MILU-CG method, is recommended.

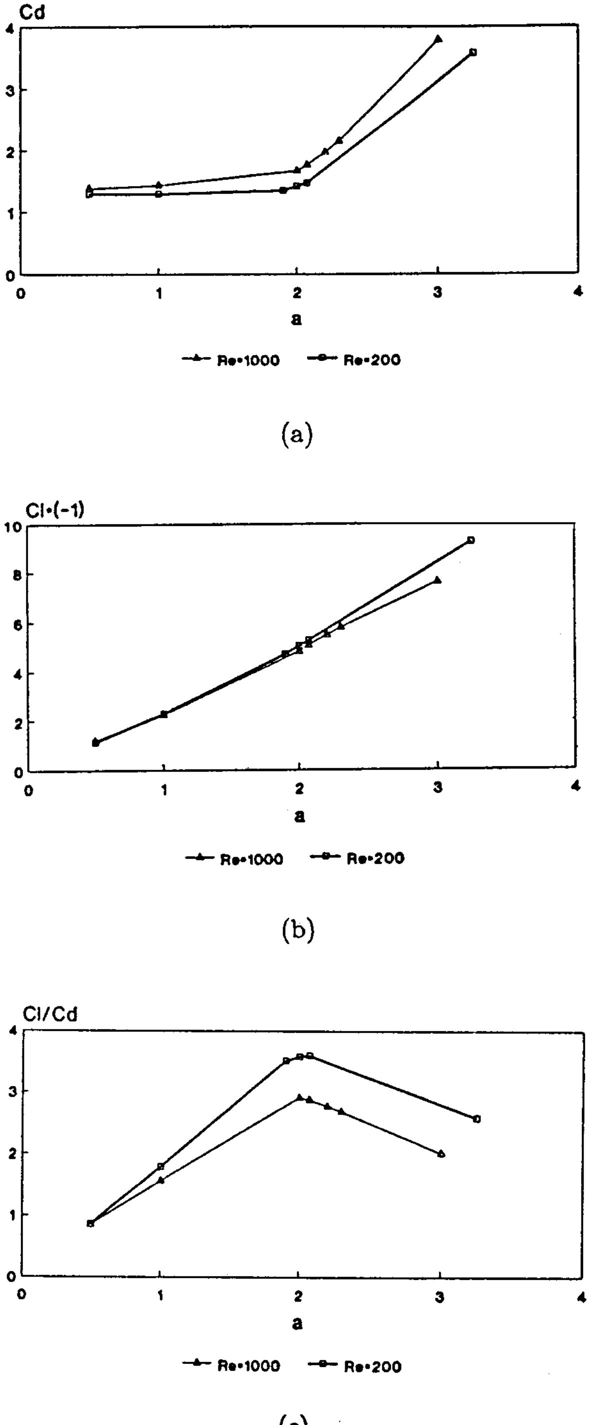

Figure 14. The variations of (a) the mean drag force coefficient $\overline{C_d}$; (b) the mean lift force coefficient $\overline{C_l}$; (c) the mean lift-to-drag force ratio $\overline{C_l}/\overline{C_d}$ with respect to α for $Re = 1000$ and 200.

ACKNOWLEDGMENTS

The authors wish to thank the anonymous referees for valuable comments that improved the presentation of the paper. This work is supported by the Natural Science Foundation of Province Jiangsu of China, and the Hong Kong RGC Earmarked Grant No. 354/018.

REFERENCES

1. M. Coutanceau and C. Menard, ‘Influence of rotation on the near-wake development behind an impulsively started circular cylinder’, *J. Fluid Mech.*, **158**, 399–446 (1985).
2. H.M. Badr and S.C.R. Dennis, ‘Time-dependent viscous flow past an impulsively started rotation and translating circular cylinder’, *J. Fluid Mech.*, **158**, 447–488 (1985).
3. H.M. Badr, M. Coutanceau and S.C.R. Dennis *et al.*, ‘Unsteady flow past a rotating circular cylinder at Reynolds numbers 10^3 and 10^4’, *J. Fluid Mech.*, **220**, 459–484 (1990).
4. C.C. Chang and R.L. Chern, ‘Vortex shedding from an impulsively started rotating and translating circular cylinder’, *J. Fluid Mech.*, **233**, 265–298 (1991).
5. Y.M. Chen, Y.R. Ou and A.J. Pearlstein, ‘Development of the wake behind a circular cylinder impulsively started into rotating and rectilinear motion’, *J. Fluid Mech.*, **253**, 449–484 (1993).
6. Y.R. Ou, ‘Mathematical modeling and numerical simulation in external flow control’, in M.D. Gunzburger (ed.), *Flow Control*, Berlin, Springer, 1995, pp. 219–255.
7. Y.T. Chew, M. Cheng and S.C. Luo, ‘A numerical study of flow past a rotating circular cylinder using a hybrid vortex scheme’, *J. Fluid Mech.*, **299**, 35–71 (1995).
8. G.H. Cottet, ‘A partical-grid superposition method for the Navier–Stokes equations’, *J. Comput. Phys.*, **89**, 301–318 (1990).
9. J.L. Guermond, S. Huberson and W.Z. Shen, ‘Simulation of two-dimensional external viscous flows by means of a domain decomposition method’, *J. Comput. Phys.*, **108**, 343–352 (1993).
10. M.H. Chou, ‘Simulation of slightly viscous external flow by a grid-partical domain decomposition method’, *Comput. Fluids*, **24**, 333–347 (1995).
11. Guo-can Ling, Guo-ping Ling and Yun-ping Wang, ‘Domain decomposition hybrid method for numerical simulation of bluff body flows’, *Sci. China (Series A)*, **35**, 977–990 (1992).
12. Guo-can Ling, Guo-ping Ling and Qi-yang Gu, ‘A new numerical method for computing the separated flow around a bluff body at high Reynolds number’, *J. Huazhong Univ. Sci Technol.*, **20**, 87–93 (1992).
13. Guo-ping Ling and Guo-can Ling, ‘A numerical study of the vortex motion in oscillating flow around a circular cylinder at low and middle *Kc* numbers’, *Acta Mech. Sin.*, **10**, 212–219 (1994).
14. Guo-ping Ling and Guo-can Ling, ‘Numerical simulations of vortex motion patterns in oscillating flow around a circular cylinder’, *Chin. J. Comput. Phys.*, **13**, 73–78 (1996).
15. Tao Lu, T. M. Shih and C.B. Liem, *Domain Decomposition Method*, Science Press, Beijing, 1992.
16. T.M. Shih, C.B. Liem and X.Y. Yue, ‘The application of MILU-CG method to three-dimensional and three phase black oil model simulations’, *Pet. Explor. Dev.*, **21**, 52–58 (1994).
17. A.B. Ebiana and R.W. Bartholomew, ‘Design considerations for numerical filters used in vortex-in-cell algorithms’, *Comput. Fluids*, **25**, 61–75 (1996).
18. H.J. Lugt and H.J. Haussling, ‘Laminar flow past an abruptly accelerated elliptic cylinder at 45° incidence’, *J. Fluid Mech.*, **65**, 711–734 (1974).